AGU ADVANCING EARTH AND SPACE SCIENCE

Geophysical Research Letters

RESEARCH LETTER
10.1029/2021GL093438

The Ekman Streamfunction and the Eulerian and Residual Overturning Circulations of the Southern Ocean

K. D. Stewart[1], A. McC. Hogg[1,2], M. H. England[2,3], D. W. Waugh[4,5], and A. E. Kiss[1]

[1]Research School of Earth Sciences, Australian National University, Canberra, ACT, Australia, [2]Australian Research Council Centre of Excellence for Climate Extremes, Sydney, NSW, Australia, [3]Climate Change Research Centre, University of New South Wales, Sydney, NSW, Australia, [4]Department of Earth and Planetary Sciences, Johns Hopkins University, Baltimore, MD, USA, [5]School of Mathematics and Statistics, University of New South Wales, Sydney, NSW, Australia

Key Points:

- We examine the relationship between the Ekman streamfunction and the Eulerian and residual Southern Ocean overturning circulations (SOOCs)
- The Ekman streamfunction and SOOC exhibit striking similarities in both latitude and density spaces
- Where the wind stress curl changes sign, the Ekman streamfunction variability coincides with >4 Sv changes in the overturning circulation

Correspondence to:
K. D. Stewart,
kial.stewart@anu.edu.au

Citation:
Stewart, K. D., Hogg, A. M., England, M. H., Waugh, D. W., & Kiss, A. E. (2021). The Ekman streamfunction and the Eulerian and residual overturning circulations of the Southern Ocean. *Geophysical Research Letters*, *48*, e2021GL093438. https://doi.org/10.1029/2021GL093438

Received 17 MAR 2021
Accepted 13 AUG 2021

Abstract The Ekman streamfunction is a wind-derived metric that can be used to infer the Southern Ocean overturning circulations (SOOCs) in both latitude-depth and latitude-potential density spaces. The Ekman streamfunction integrates the Ekman pumping zonally and northwards from Antarctica, either to a given latitude or potential density. Here, we evaluate the relationship between the Ekman streamfunction and SOOCs in a global 0.1° ocean-sea-ice model driven by interannual forcing (1958–2018). In certain regions of the Southern Ocean, strong correlations ($r > 0.9$) exist between the Ekman streamfunction and the Eulerian and residual SOOCs on monthly and annual timescales. Regression analysis identifies regions where Ekman streamfunction variability coincides with > 4 Sv changes in the overturning; one such location is where the wind stress curl changes sign and the Ekman pumping is highly variable.

Plain Language Summary The global ocean overturning circulation is the planetary-scale movement of waters in the vertical and north-south directions. It is the principal mechanism by which the oceans absorb, sink, and redistribute heat and carbon from the atmosphere, thereby regulating Earth's climate. Despite its importance, it is impossible to observe directly, and must be inferred from sparse and infrequent proxy measurements. The main upward branches of the overturning circulation are located in the Southern Ocean, where strong westerly winds upwell waters from below. Thus, changes in these westerly winds will lead to changes in the overturning circulation, and, subsequently, Earth's climate. Here, we employ a diagnostic tool, called the Ekman streamfunction, to cast the change of the winds into a framework that is directly comparable with the overturning circulation. We use a state-of-the-art global ocean-sea-ice model, in which the overturning circulation is measured directly, to examine the relationship between the Ekman streamfunction and the Southern Ocean overturning circulation. We find that throughout much of the Southern Ocean, the Ekman streamfunction is a robust indicator of the strength and variability of the overturning circulation, with exceptionally high correlation.

1. Introduction

The role that the global oceans play in Earth's climate is governed by the Southern Ocean and its overturning circulation (Sallèe, 2018). The Southern Ocean overturning circulation (SOOC) maintains the bulk stratification of the global oceans through the replenishment of abyssal, deep and mode waters in all major ocean basins (Marshall & Speer, 2012). The SOOC is the primary process by which the oceans sequester excess heat and carbon from the atmosphere, thereby regulating climate conditions globally (Roemmich et al., 2015; Sabine et al., 2004). Thus, changes in the SOOC, anthropogenic or otherwise, will have substantial ramifications for the trajectory of Earth's climate. Quantifying the magnitude of the SOOC and its variability, however, remains a challenge; direct observation of the overturning circulation is not possible, and the few proxy measurements of the SOOC are infrequent, sparse, and with large uncertainties. Any scientific developments that grant insight into the SOOC and its dynamics are most welcome.

The SOOC, along with the Atlantic and global meridional overturning circulations, are the result of a complicated interplay between surface buoyancy forces, wind stress, and turbulent mixing, the effects of which, in turn, depend on one another (Johnson et al., 2019; Marshall & Speer, 2012). This intrinsically coupled

nature of the SOOC forcing makes it impossible to decompose the overturning into its separate buoyancy-driven, wind-driven, and mixing-driven components. Nevertheless, it is both possible and illuminating to diagnose and consider the effects of relative changes in the distinct forces that drive the SOOC, especially since these forces have recently exhibited trends. For example, the midlatitude westerly winds over the Southern Ocean, often characterized by the Southern Annular Mode (SAM) index, have strengthened and shifted poleward during the recent decades (e.g., Goyal et al., 2021). Understanding the oceanographic consequences of these trends in the Southern Hemisphere winds, especially in regards to the response of the SOOC, will greatly improve climate projections.

The link between the Southern Hemisphere winds and the SOOC has received much scientific attention over the past several decades (e.g., see reviews by Gent, 2016). The substantial body of research in this field highlights the important distinction between the SOOC in latitude-depth space and in latitude-potential density space (e.g., Döös & Webb, 1994), and identifies correlations between the strength of the wind forcing and the SOOC (e.g., Tandon et al., 2020). It also establishes that the principal dynamical constraint imposed by the open Drake Passage is that there can be no geostrophically balanced meridional flow at these zonally uninterrupted latitudes, requiring the local northward flow of the upper ocean, and the subsequent return flow of the deeper ocean, to be a result of wind forcing, thereby intrinsically linking the SOOC and the wind forcing at these latitudes (known as the "Drake Passage Effect"; Toggweiler & Samuels, 1995). Directly relating the changes in the SOOC transport streamfunction (in Sverdrups, Sv; where 1 Sv $= 10^6$ m^3/s) to the changes in the wind stress (N/m^2) requires the influence of the wind forcing to be cast as an effective ocean transport, which is achieved by way of Ekman theory (e.g., Karsten & Marshall, 2002; Mazloff et al., 2013; Olbers & Visbeck, 2005; Sallèe et al., 2010; Speer et al., 2000; Treguier et al., 2007). That is, the meridional Ekman transport, or vertical Ekman pumping, which are both functions of the wind stress, can be spatially integrated to return an estimate of the wind-driven circulation, which we refer to here as the Ekman streamfunction. This Ekman streamfunction methodology can then be implemented in a wide range of scientific approaches to investigate the response of the SOOC to changes in the Southern Hemisphere winds.

Here, we examine the relationship between the SOOC and the Ekman streamfunction, which we define in Section 2. This Ekman streamfunction theoretically quantifies the mechanical forcing of the winds on the ocean; it does not incorporate the wind-driven buoyancy or mixing components, or their successive feedbacks. The Ekman streamfunction here is defined in such a way that it is convenient to implement in practice, and directly equivalent to the SOOC, in both latitude-depth and latitude-potential density spaces. In Section 3, we detail the high-resolution global ocean-sea-ice model which we use to evaluate the relationship between the Ekman streamfunction and the SOOC. We present and discuss our findings in Section 4, and summarize our conclusions in Section 5.

2. Theory

The SOOC can be characterized in terms of its Eulerian streamfunction in latitude-depth space, and its residual streamfunction in latitude-potential density space (e.g., J. Marshall & Radko, 2003; Zika et al., 2012). The local cartesian coordinates for the zonal, meridional, and vertical directions are given by x, y, and z (m), respectively, with the potential density as σ_2 (kg/m^3), which is the potential density of seawater referenced to 2,000 dbar less 1,000 kg/m^3. The Eulerian streamfunction can be developed by integrating the vertical velocity w (m/s) in both the zonal direction and in the meridional direction from a southern latitude located entirely inside the Antarctic continent northwards to a given latitude corresponding to y:

$$\Psi_w\left(y,z,t\right) = \int_{A_y} w\left(x,y',z,t\right) dA, \tag{1}$$

where A_y is the zonal-meridional surface area for latitudes corresponding to $y' < y$. The Eulerian streamfunction is usually defined in terms of the meridional velocity, v, integrated in both the zonal direction and vertically from the ocean bottom to a given depth; however, the definition in Equation 1 is mathematically equivalent and has a more direct application to our subsequent analysis.

In a similar manner, the residual streamfunction is developed by integrating the meridional velocity, v, in both the zonal direction and vertically from the bottom of the ocean upwards to a depth z where the potential density reaches a given value σ_2 (assuming a stable stratification):

$$\Psi_{\sigma_2}\left(y,\sigma_2,t\right) = \int_{A_{\sigma_2}} v\left(x,y,z,t\right) dA, \tag{2}$$

where A_{σ_2} is the cross-sectional area in the zonal-depth plane of the potential densities $\sigma_2' > \sigma_2$. Compared to the Eulerian streamfunction, the residual streamfunction is more important for Earth's climate as it represents the meridional exchanges of water properties in potential density space (e.g., Zika et al., 2012).

The vertical velocity associated with Ekman pumping w_{Ek} (m/s) at the base of the surface Ekman layer can be estimated by taking the curl of the wind stress $\boldsymbol{\tau}$ (N/m^2), as:

$$w_{Ek}\left(x,y,t\right) = \boldsymbol{k} \cdot \nabla \times \left(\frac{\boldsymbol{\tau}\left(x,y,t\right)}{\rho_0 f(y)} \right), \tag{3}$$

where, ρ_0 is the reference seawater density, $f(y)$ is the local Coriolis parameter, and $\boldsymbol{k}$ is the vertical unit vector. The Ekman pumping velocity w_{Ek} is a wind-derived metric that should only be considered as a theoretical estimate of the actual vertical velocities; for instance, it does not account for vertical velocities arising from buoyancy-driven convection. However, estimates of $\boldsymbol{\tau}$, and thus w_{Ek}, are obtainable from satellite-derived global data sets of wind stress.

Following the approach in Equation 1, where the model-diagnosed vertical velocity w is used to develop the Eulerian streamfunction, we take the Ekman pumping velocity w_{Ek} and integrate it zonally and meridionally in a similar fashion:

$$\Psi_{Ek}\left(y,t\right) = \int_{A_y} w_{Ek}\left(x,y',t\right) dA. \tag{4}$$

We refer to Ψ_{Ek} as the Ekman streamfunction. As per alternative definitions for the wind-driven overturning circulation, Ψ_{Ek} can be thought of as an estimate of the Eulerian overturning circulation at the base of the surface Ekman layer due to Ekman pumping (e.g., Treguier et al., 2007).

We can further extend the analysis of the Ekman streamfunction from latitude space into potential density space by integrating the Southern Hemisphere w_{Ek} in both the zonal and meridional directions where the surface potential density is greater than a given value of σ_2:

$$\Psi_{Ek}^{\sigma_2}\left(\sigma_2,t\right) = \int_{A^{\star}_{\sigma_2}} w_{Ek}\left(x,y,t\right) dA, \tag{5}$$

where $A^{\star}_{\sigma_2}$ is the outcrop surface area of potential densities $\sigma_2' > \sigma_2$, and the superscript σ_2 denotes $\Psi_{Ek}^{\sigma_2}$ is in surface σ_2-space. Note that in this instance, σ_2 serves as a pseudo-meridional coordinate as the surface potential density approximately scales with latitude. This definition of the wind-driven overturning circulation in potential density space is similar to previous definitions for such a diagnostic (e.g., Lee & Nurser, 2012). We refer to $\Psi_{Ek}^{\sigma_2}$ as the Ekman streamfunction in density coordinates.

While the definitions of the Ekman streamfunctions above use the Ekman pumping velocity calculated from the wind stress curl, it is mathematically equivalent to use the divergence of the Ekman transport in the surface Ekman layer, $\boldsymbol{u}_{Ek} = (\tau_y, -\tau_x)/(\rho_0 f)$. That is, following on from Equations 3 and 4:

$$\Psi_{Ek}\left(y,t\right) = \int_{A_y} w_{Ek}\left(x,y',t\right) dA = \int_{A_y} \boldsymbol{k} \cdot \nabla \times \left(\frac{\boldsymbol{\tau}\left(x,y',t\right)}{\rho_0 f\left(y'\right)} \right) dA = \int_{A_y} \nabla \cdot \boldsymbol{u}_{Ek}\left(x,y',t\right) dA. \tag{6}$$

We can apply the divergence theorem to the right hand expression to return the line integral of the Ekman transport at the latitude corresponding to y:

$$\Psi_{Ek}\left(y,t\right) = \int_{A_y} \nabla \cdot \boldsymbol{u}_{Ek}\left(x,y',t\right) dA = \oint \boldsymbol{u}_{Ek}\left(x,y,t\right) \cdot \mathbf{n} dl = -\int \frac{\tau_x\left(x,y,t\right)}{\rho_0 f(y)} dx, \tag{7}$$

where **n** is the horizontal unit vector normal to the line of latitude corresponding to y. Equation 7 states that the Ekman streamfunction at the latitude corresponding to y represents the integral of the Ekman transport normal to y, which is equivalent to the total meridional Ekman transport at y. Thus, the Ekman streamfunction at a given latitude is simply a function of the zonal wind stress at that latitude, which is a commonly used metric to represent the wind-driven overturning circulation (e.g., Tandon et al., 2020). This case is triv-

ial because the horizontal unit vector **n** normal to the bounding latitude corresponding to y is, by definition, purely in the meridional direction. However, if the boundary of the area integral is not aligned with the geometric coordinates, or varies in time, or is discontinuous in space, as is the case for outcropping potential density surfaces in Equation 5, defining the Ekman streamfunction in terms of the line integral of the wind stress becomes impractical. Therefore, because of the simplicity and consistency of the definitions of the Ekman streamfunctions in Equations 4 and 5, and the intuitive and direct comparisons that these definitions facilitate between the Ekman streamfunctions and the overturning circulations, it is convenient to use the wind stress curl to calculate the Ekman pumping and subsequently both of the Ekman streamfunctions.

3. Model and Methodology

We employ output from the 0.1° configuration of the Australian Community Climate and Earth System Simulator ocean model version 2 (ACCESS-OM2-01; Kiss & Hogg, 2020; Kiss et al., 2020), the flagship ocean-sea-ice model of the Consortium for Ocean-Sea-Ice Modeling in Australia (COSIMA) run on the Gadi Supercomputer (NCI Australia, 2019). ACCESS-OM2-01 uses a generalized $z z^*$ coordinate with vertical grid spacings that have been objectively constructed to support the vertical structure of the baroclinic dynamics permitted by the horizontal grid (Stewart et al., 2017), and does not use sub-grid-scale parameterizations for mesoscale eddies. The ACCESS-OM2-01 simulation is initialized with January temperature and salinity fields from the World Ocean Atlas 2013 v2 monthly climatology (WOA13; Locarnini et al., 2013; Zweng et al., 2013), and forced with prescribed atmospheric conditions taken from the Japanese atmospheric reanalysis data set for driving ocean models (JRA55-do v1.4; Tsujino et al., 2018). These prescribed atmospheric conditions are the interannual forcing (JRA55-do-IAF) that runs 61 years from 1958 to 2018, inclusive. Two cycles of the JRA55-do-IAF are imposed in serial, such that in the second cycle there is a sudden transition at the end of December 31, 2018 back to the start of January 1, 1958, as per the forcing protocol of Ocean Model Intercomparison Project phase 2 (OMIP2; Tsujino et al., 2020).

We analyze monthly means to evaluate the two overturning streamfunctions and the two Ekman streamfunctions, as detailed in Section 2. Due to the dominance of the seasonal signal in these terms, it is necessary to first de-season the monthly mean output by removing the average of the entire two JRA55-do-IAF cycles of a given month from that given month (i.e., the average state of the 122 Januarys are removed from each January, and so on, for each of the 12-months). Our analysis then focusses on the comparison of the four streamfunctions at two temporal scales: (a) the de-seasoned monthly means, and (b) the 12 months running averages.

To quantify the relationships between the streamfunctions, we calculate the respective correlation coefficients, r, between the time series of the Ekman streamfunctions and the overturning streamfunctions at zero lag. Considering the high degree of autocorrelation in these streamfunctions, it is necessary to perform a statistical significance test that uses an effective sample size N_{eff}, given by:

$$N_{eff} = N\left(\frac{1 - r_1 r_2}{1 + r_1 r_2}\right), \tag{8}$$

where N is the actual sample size ($N = 1464$ months), and r_1 and r_2 are the lag-1 autocorrelations of the two time series of interest (e.g., see Santer et al., 2000). Note that the effective sample size N_{eff} varies spatially. As a measure for statistical significance we use the student's t-distribution to identify where $r\sqrt{N_{eff}} \,/\, \sqrt{1 - r^2} > 1.96$, which corresponds to regions where the correlation is significant at the 95% level such that the null hypothesis is rejected.

We also perform the following linear regression analyses:

$$\Psi_w\left(y,z,t\right) = \gamma^w_{Ek}\left(y,z\right)\Psi_{Ek}\left(y,t\right) + c_1, \tag{9}$$

and,

$$\Psi_{\sigma_2}\left(y,\sigma_2,t\right) = \gamma^{\sigma_2}_{Ek}\left(y,\sigma_2\right)\Psi^{\sigma_2}_{Ek}\left(\sigma_2,t\right) + c_2, \tag{10}$$

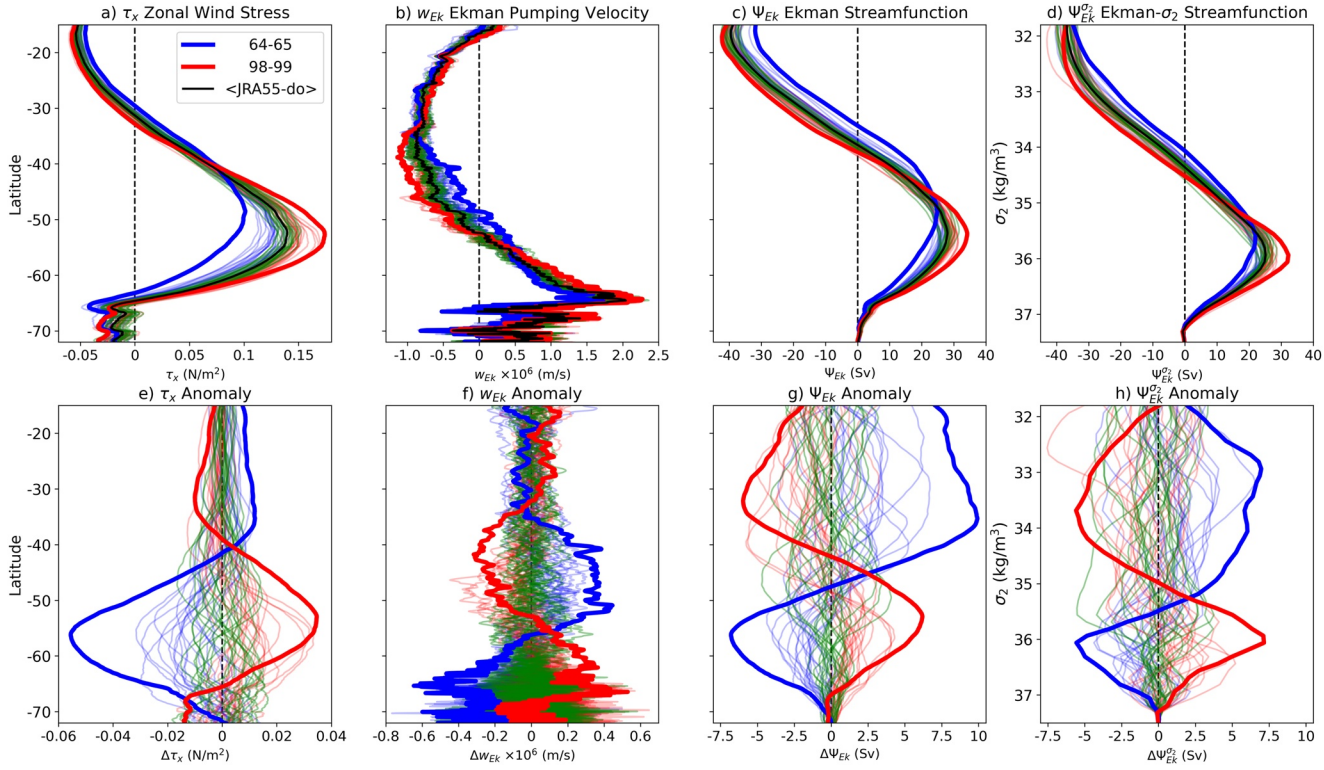

Figure 1. Zonal means of the July–June averages for the (a) Zonal wind stress, (b) Ekman pumping velocity, (c) Ekman streamfunction, all calculated from the second cycle of the JRA55-do-IAF, along with their respective anomalies from the cycle mean (e–g). The thicker blue and red lines denote two end-member cases of extremely weak and strong wind forcing, corresponding to July 1964 – June 1965 (64–65) and July 1998 – June 1999 (98–99), respectively, with the black lines showing the mean of the second JRA55-do-IAF cycle (<JRA55-do>). The faint lines are included to be indicative of the extent of variability in these fields; these are colored blue, green, and red, indicating weak, neutral, and strong forcing conditions, respectively. Equivalent depictions of the (d) Ekman streamfunction in density coordinates, and its (h) anomaly, plotted as a function of the outcropping potential density σ_2.

where the regression coefficients γ^{w}_{Ek} and $\gamma^{\sigma_2}_{Ek}$ represent the change in overturning streamfunctions coincident with unit changes in Ekman streamfunctions.

The correlation and regression analyses are performed on the de-seasoned monthly means and 12 months running averages of the streamfunctions for the entire two JRA55-do-IAF cycles of the ACCESS-OM2-01 simulation, returning distributions of correlations and linear regression coefficients in latitude-depth and latitude-potential density space. For the regression analysis, in order to better gauge the magnitude of the overturning circulation anomalies indicated by the coefficients $\gamma^{w}_{Ek}(y,z)$ and $\gamma^{\sigma_2}_{Ek}(y,\sigma_2)$, we scale them by the standard deviations of the respective Ekman streamfunctions $std\left(\Psi_{Ek}(y)\right)$ and $std\left(\Psi^{\sigma_2}_{Ek}(\sigma_2)\right)$. These scaled regression coefficients $std\left(\Psi_{Ek}\right)\cdot\gamma^{w}_{Ek}$ and $std\left(\Psi^{\sigma_2}_{Ek}\right)\cdot\gamma^{\sigma_2}_{Ek}$ thus represent the magnitude of the change in overturning streamfunctions, in Sverdrups, that is coincident with a one standard deviation change in the Ekman streamfunction.

4. Results and Discussion

The zonal means of the July–June averages of zonal wind stress τ_x highlights the considerable variability in both the latitude of the peak wind stress (48–54°S), and its magnitude (0.9–0.17 N/m^2), with periods of weaker forcing conditions (blue lines) tending to peak relatively further north (Figure 1a). This range of variability in both the latitude and magnitude of the peak zonal wind stress is consistent with previous analysis of reanalyzes and models (e.g., Swart & Fyfe, 2012). Using the 61 yr average of the second JRA55-do-IAF cycle as a reference (referred to as <JRA55-do>), the peaks in the zonal wind stress anomalies also exhibit

considerable variability, with typical magnitudes of ±25% (±0.03 N/m^2) of the average zonal wind stress, and more than 40% decrease for the period July 1964–June 1965 (64–65; Figure 1e).

The Ekman pumping velocities also exhibit considerable interannual variability in their magnitude and latitudinal distribution (Figure 1b). Here, negative w_{Ek} arises when there is a convergence of surface waters, reflecting a downward motion of water driven by the wind stress, with positive w_{Ek} indicating upwelling; these are often referred to as Ekman pumping and Ekman suction, respectively. The interannual variability of the zero-crossing latitude of w_{Ek}, which approximately corresponds to the latitude of peak τ_x, indicates that these latitudes (48–54°S) can experience both upwelling and downwelling on a year-to-year basis and thus are likely to exhibit substantial variability in their hydrographic properties. Strong forcing conditions (red lines) are associated with an enhancement of both upwelling and downwelling velocities. The Ekman pumping velocity anomalies are largest in regions prone to seasonal sea-ice (south of 65°S); north of the sea-ice, the interannual anomalies span $\pm 0.4 \times 10^{-6}$m/s, which for some latitudes (~45–60°S) can be larger than the average w_{Ek} velocity (Figure 1f).

The Ekman streamfunction (Equation 4) peaks between ~27–35 Sv centered around 50°S, where w_{Ek} changes sign (Figure 1c); this is consistent with observation-based estimates of similarly defined Ekman transports (e.g., Olbers & Visbeck, 2005; Sallée et al., 2010). The two end-member cases of weak and strong wind forcing envelop the range of Ekman streamfunctions from the second cycle of JRA55-do-IAF. Note that while the Ekman streamfunction is developed from the comparatively noisy Ekman pumping velocity w_{Ek}, being a double area integral the Ekman streamfunction is smooth and well-behaved; this is particularly the case for the seasonal sea-ice regions where the substantial variability of the Ekman pumping velocity is muted by its relatively small areal extent. The Ekman streamfunction anomalies (Figure 1g) span the range −7 to +10 Sv; strong forcing conditions tend to have positive anomalies to the south of ~50°S, and negative anomalies to the north, which is mirrored for weak forcing conditions.

There are similarities between the distributions and magnitudes of the two Ekman streamfunctions (Figures 1c and 1d); they both initially increase toward northern/lighter outcropping waters, with the Ekman streamfunction in density coordinates peaking between ~22–33 Sv around $\sigma_2 = 35.8 kg/m^3$. The similar distributions of the Ekman streamfunctions here demonstrate the close relationship between latitude and outcrop potential density on an annual timescale, and extend to the anomalies of the Ekman streamfunction in density coordinates (Figure 1h).

To examine the relationship between the Ekman streamfunction and the model-diagnosed SOOC, we first focus on the Eulerian case (Figure 2). The Eulerian streamfunction anomalies primarily depend on latitude, and are consistent with the Ekman streamfunction anomalies (overlying sub-panels of Figures 2a and 2b) in both latitudinal distribution and magnitude but with some differences: the magnitude of the anomalous Ekman streamfunction is weaker (stronger) than the Eulerian streamfunction in the south (north), and the latitude of the Ekman streamfunction zero anomaly is displaced south. The strong, vertically coherent, latitudinal dependence reflects the rapid and deep penetrating response of the Southern Ocean circulation to variations in the wind stress.

Time series of the Eulerian and Ekman streamfunctions at a given location further demonstrate their close resemblance and offer an indication of their relative magnitudes and behaviors (Figure 2c). At 50°S and 1 km depth, the 12 months running averages of the Eulerian and Ekman streamfunctions are of similar magnitude, and with a correlation of $r^w_{Ek} = 0.78$. Note that this close agreement in magnitude is not necessarily representative of other locations throughout the Southern Ocean. Interestingly, both cycles of the JRA55-do-IAF exhibit a long-term trend in the streamfunctions from a minimum around 1964–65 to a maximum around 1998–99 (which happen to coincide with the two extreme end-member periods), where the streamfunctions increase by approximately 8 Sv each (equivalent to 2.3 Sv/decade); the timing of this long-term trend is consistent with that of the observation-based SAM index (Marshall, 2003).

To understand the extent to which this strong relationship extends throughout the Southern Ocean, we examine the distribution of r^w_{Ek}. On the monthly timescale, there is a high correlation ($r^w_{Ek} > 0.5$) down to 4 km depth and north to 20°S (Figure 2d). The region between 65 and 55°S exhibits the strongest correlation ($r^w_{Ek} > 0.9$), with a second, relatively weaker local maxima of $r^w_{Ek} > 0.7$ apparent between 45 and 35°S and

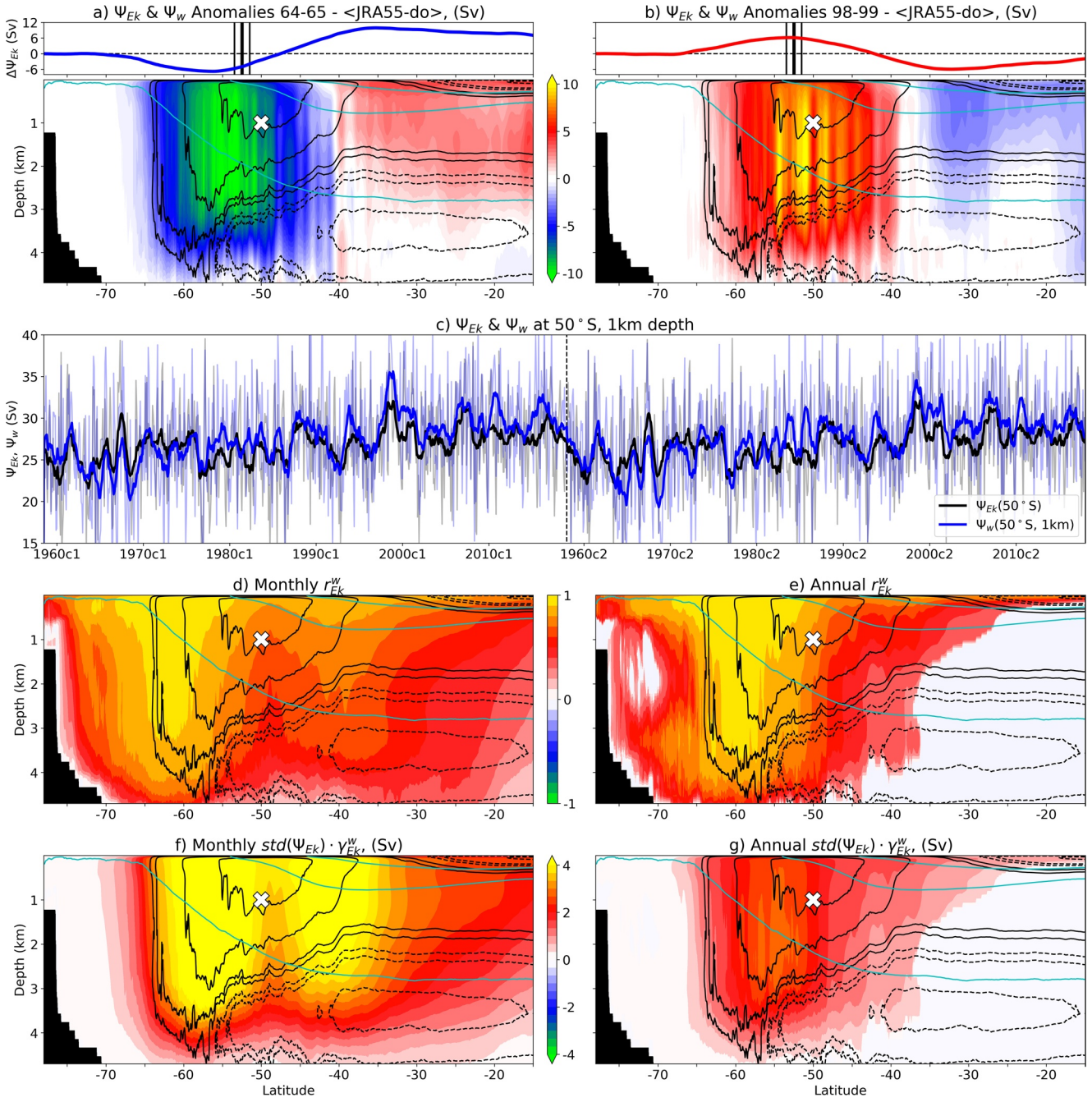

Figure 2. The Eulerian streamfunction anomalies (color shaded) for the periods (a) July 1964 – June 1965 and (b) July 1998 – June 1999, relative to the mean of the second cycle of JRA55-do-IAF, with their respective Ekman streamfunction anomalies included for reference (lines in upper panels). The <JRA55-do > mean Eulerian streamfunction is contoured in black at ±2.5, 5, 15, 25 Sv intervals with the circulation going clockwise (anticlockwise) around the solid (dashed) contours. The $\sigma_2 = 35, 36, 37$ kg/m^3 isopycnals of <JRA55-do> are shown in cyan. The black lines in the upper panels indicate the latitudinal location of the <JRA55-do> Ekman streamfunction maximum (thick) and its annual standard deviation (thin). Panel (c) presents time series over both cycles (separated by the vertical dashed line) of the Eulerian and Ekman streamfunctions at 50°S and 1 km depth; this location is denoted by the white crosses in the other panels. The bold lines are the 12 months running averages; faint lines are the monthly means included so as to be indicative of the intra-annual variability. Distributions of the statistically significant correlation coefficients r^w_{Ek} and the scaled regression coefficients $std\left(\Psi_{Ek}\right) \cdot \gamma^w_{Ek}$ calculated from the (d, f) de-seasoned monthly means and (e, g) 12 months running averages. The black and cyan contours, and the white crosses, are the same as for panels (a, b).

reaching 2 km depth. The strong correlations at zero lag in these regions reflect the rapid response of the Eulerian streamfunction to the wind-driven variability, which is evidently being captured by the Ekman streamfunction.

Widening the temporal scale to the 12 months running averages has the effect of reducing the strength of the correlation north of 50°S, and increasing it between 65 and 50°S (Figure 2e). The region with a strong correlation of $r^{w}_{Ek} > 0.7$, between 65 and 50°S and down to 4 km depth, corresponds to the upwelling flank of the "Deacon cell," a localized wind-driven overturning of waters in Eulerian space with near-uniform properties such that it does not contribute to the meridional transport of tracer (e.g., Farneti et al., 2015; Zika et al., 2012). The regions with statistically significant correlations shallows from 4.5 km deep at around 50°S to 500 m depth at 25°S; north of this, the regions of significance are confined to the surface waters only. The region with the strongest correlation of $r^{w}_{Ek} > 0.9$ spans the latitudes of the Drake Passage (62–55°S), and is likely a natural consequence of the Drake Passage Effect (Toggweiler & Samuels, 1995).

To understand the relative magnitudes of the Eulerian and Ekman streamfunction covariances, we examine the scaled regression coefficient $std\left(\Psi_{Ek}\right) \cdot \gamma^{w}_{Ek}$, which is indicative of the magnitudes of Eulerian streamfunction anomaly (in Sverdrups) that occur coincident with one standard deviation change in the Ekman streamfunction. For the de-seasoned monthly means, the scaled regression distribution is greater than 2 Sv north of the seasonal sea-ice regions (65°S) and down to a depth of 4 km, with two distinct maxima of over 4 Sv centered at 57°S and 40°S (Figure 2f). These two maxima coincide with the up- and downwelling branches of the Deacon cell, evident by the closed circulation contours of the Eulerian streamfunction. The magnitude of the scaled regression decreases as the temporal scale is widened to the 12 months running average (Figure 2g), in part due to the reduction in the standard deviation of the longer-term averaged Ekman streamfunction. The maximum annual scaled regression occurs between 60 and 50°S and down to 4 km depth, and in places reaching over 3 Sv. The northern maximum around 40°S in the de-seasoned monthly means is not evident in the longer temporal average. As with the equivalent correlation distribution (Figure 2e), the strongest positive region corresponds to the upwelling branch of the Deacon cell, reflecting the ability of the Ekman streamfunction to represent the effect of wind stress variability on this wind-driven circulation feature.

While the correlations between the Eulerian and Ekman streamfunctions are both strong and deep-reaching, the Eulerian overturning circulation does not necessarily correspond to property transports, especially in the Southern Ocean (Zika et al., 2012). The residual streamfunction, in contrast, represents the meridional exchanges of water masses in potential density space, and is substantially more important for Earth's climate. While the traditional coordinates of the residual streamfunction span latitude-potential density space, for ease of comparison with the Eulerian streamfunction here we interpolate the residual streamfunction into latitude-depth space, and the Ekman streamfunction in density coordinates into latitude space (Figures 3a and 3b). Note that these interpolations are for the purposes of plotting only; the following correlation and regression analyses are performed in latitude-potential density space. The magnitude and distribution of the residual streamfunction anomaly fields are largely consistent with those of the Ekman streamfunction anomalies, especially between 60 and 40°S. The strong, vertically coherent latitudinal dependence of the residual streamfunction anomaly distributions, which is also present in the Eulerian streamfunction anomaly distributions (Figures 2a and 2b), again reflects the rapid and deep response of the Southern Ocean to variations in the wind forcing. In the vicinity of the outcrop of $\sigma_2 = 36\text{kg/m}^3$, which is at approximately 52°S and coincides with the change of sign of the wind stress curl, there is evidence of strong anomaly signals penetrating from the surface into the interior along isopycnals (i.e., aligned with the cyan contours) and reaching northwards of 45°S.

As for the Eulerian case, we select a location in latitude-potential density space (50°S and $\sigma_2 = 36.4\text{kg/m}^3$) and present the time series of the residual and Ekman streamfunctions in density coordinates (Figure 3c). At this location, the Ekman streamfunction is always larger than the residual streamfunction, which initially starts at rest. The correlation between the residual and Ekman streamfunctions at this location is $r^{\sigma 2}_{Ek} = 0.64$, which is slightly weaker than that of the Eulerian and Ekman streamfunctions ($r^{w}_{Ek} = 0.78$; Figure 2c); this reflects the different processes by which the wind stress variability signal propagates through the Eulerian and residual overturning circulations. That is, in the Eulerian case the wind variability signal

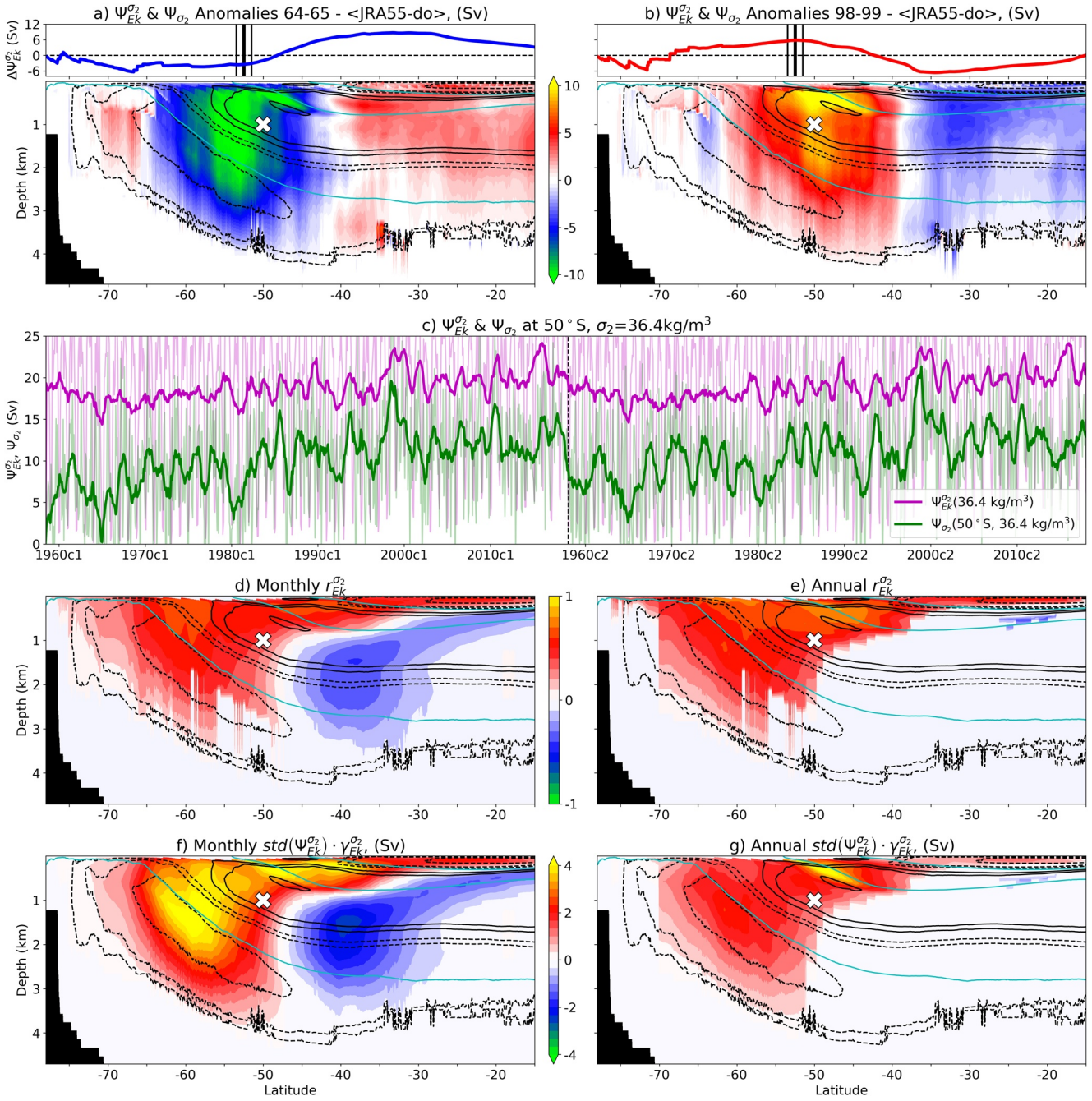

Figure 3. As for Figure 2, only showing the residual streamfunction anomalies (color shaded) with their respective anomalies of the Ekman streamfunction in density coordinates (upper panels) for reference. Panel (c) presents time series of the residual and Ekman streamfunctions at 50°S and σ_2 = 36.4kg/m^3 (white crosses in other panels). Panels (d, e) show the distributions of the statistically significant correlation coefficients $r^{\sigma_2}_{Ek}$ for the de-seasoned monthly means and 12 months running averages, respectively, and panels (f, g) show their scaled regression coefficients $std\left(\Psi^{\sigma_2}_{Ek}\right) \cdot \gamma^{\sigma_2}_{Ek}$. To facilitate comparison with Figure 2, the residual and Ekman streamfunctions in density coordinates have been interpolated into latitude-depth space.

propagates vertically into the ocean via the barotropic mode, tending to have a near-immediate and full-depth response; in the residual case, the wind variability signal propagates into the interior along isopycnals, which tends to be a slower process. Note that while the long-term trend that was evident in the Eulerian case between 1964–65 and 1998–99 is also present here, the trend appears relatively weaker for the Ekman streamfunction in density coordinates (~5 Sv) and relatively stronger for the residual streamfunction (~11 Sv).

The distribution of the statistically significant correlations between the de-seasoned monthly means of the residual and Ekman streamfunctions in density coordinates (Figure 3d) exhibit a region of strong positive correlations ($r^{\sigma_2}_{Ek} > 0.6$) in the upper 500 m spanning the entire Southern Ocean, and in the upper 1 km south of 40°S. This strong correlation between the residual streamfunction in these upper waters and Ekman streamfunction in density coordinates makes sense as these waters are in direct contact with the wind forcing. The strong surface signal of the de-seasoned monthly mean correlations appears to penetrate into the ocean interior along isopycnals from the location of a given σ_2 outcrop a distance of up to 10° of latitude. In the northern region of the Southern Ocean, there is a relatively weaker negative correlation ($r^{\sigma_2}_{Ek} \approx -0.3$) signal, suggesting that on a monthly timescale the residual streamfunction anomalies here are out of phase with those of Ekman streamfunction anomalies. Extending the temporal scale to the 12 months running averages (Figure 3e) further intensifies the strong correlation ($r^{\sigma_2}_{Ek} > 0.7$) signal of the upper 1 km between 65 and 40°S. The northward penetration of the strong signal has widened from that of the de-seasoned monthly means to be approximately 15° of latitude in extent. Also, on this annual timescale, the relatively weaker negative signal evident in the de-seasoned monthly means is no longer present, suggesting the variability timescale of this feature is between monthly and annual (i.e., seasonal).

The equivalent scaled regression analysis for the de-seasoned monthly means show that $std\left(\Psi^{\sigma_2}_{Ek}\right) \cdot \gamma^{\sigma_2}_{Ek}$ is strongest (> 4 Sv) in the upper 1 km between 65 and 35°S, reaching depths of 2 km for 60–55°S, and with a relatively weaker negative signal (<−2 Sv) to the north between 45 and 35°S and 1–2.5 km depth (Figure 3f). The region with the strongest response coincides with the upwelling branch of the "upper cell," or the Atlantic meridional overturning circulation. Widening the temporal scale to the 12 months running averages reduces the breadth of the upper ocean signal, localizing the peak to a maximum of $std\left(\Psi^{\sigma_2}_{Ek}\right) \cdot \gamma^{\sigma_2}_{Ek} > 4$ Sv centered around 52°S and $\sigma_2 = 36$ kg/m^3 (Figure 3g). Note that this location in latitude-potential density space corresponds to the respective maxima of both Ekman streamfunctions; that is, this location is where the wind stress curl changes sign, which has been identified as a region that is particularly sensitive to atmospheric variability, and a hotspot for heat uptake (Stewart & Hogg, 2019).

Our focus here has been on the relationship between the Ekman streamfunctions and the Eulerian and residual overturning circulations, which themselves are related through an eddy overturning circulation (e.g., Marshall & Radko, 2003). This eddy overturning circulation, which opposes the Eulerian overturning circulation, represents the difference between the Eulerian and residual overturning circulations. An important dynamical property of the eddy overturning circulation is that its response to changes in wind forcing tend to oppose the response of the Eulerian overturning circulation, such that the residual overturning circulation is insensitive to changes in the wind forcing (known as "eddy compensation"; e.g., Downes & Hogg, 2013). The analysis presented here, however, indicates that the residual overturning circulation is indeed sensitive to the winds, albeit less sensitive than the Eulerian overturning circulation. This sensitivity is understood to be a consequence of timescales; that is, the timescale for the eddy overturning circulation to adjust and compensate the changes in the Eulerian overturning circulation is longer than the monthly or annual averages analyzed here, such that eddy compensation is ineffective here.

5. Conclusions

We have examined the relationship between the Ekman streamfunction and the variability of the SOOC in both latitude-depth and latitude-potential density spaces. The Ekman streamfunction, which is developed by integrating the vertical Ekman pumping velocities zonally and northwards from the Antarctic coastline to either a given latitude or potential density, returns a theoretical representation of the influence of the wind on the SOOC at the base of the surface Ekman layer. The primary distinguishing feature of the Ekman streamfunction as defined here to alternative metrics of the wind forcing is that it is calculated so as to be directly equivalent to the SOOC in both latitude-depth and latitude-potential density spaces. We evaluate the utility of the Ekman streamfunction as a measure of the SOOC with a global 0.1° ocean-sea-ice model, driven with interannual forcing. The results presented here highlight the close association of the Ekman streamfunction and the SOOC, and the regions and timescales where the two are directly relatable. The covariance between the Ekman streamfunction and the diagnosed Eulerian SOOC is remarkable, especially in the upwelling flank of Deacon cell, and in particular the latitudes of the Drake Passage, where the

correlation is greater than 0.9 and likely a consequence of the Drake Passage Effect. A scaled regression analysis indicates that for certain locations a one standard deviation change in the Ekman streamfunction coincides with a > 4 Sv change in the Eulerian SOOC on monthly and annual timescales, which amounts to approximately 10% of overturning. The correlation between the residual SOOC and the Ekman streamfunction in density coordinates penetrates northwards along isopycnals up to 15° of latitude within a year. The scaled regression signals peak at 52°S and σ_2 = 36 kg/m^3, which are the locations of the zero wind stress curl, reflecting the heightened sensitivity of this particular region to atmospheric variability. The strong correlations between the Ekman streamfunctions and the Eulerian and residual overturning circulations suggest that eddy compensation is ineffective on these monthly and annual timescales. The results also suggest that for regions with weak or insignificant correlations, the overturning circulation variability is due to dynamical processes other than wind forcing, such as buoyancy fluxes. In summary, this analysis clearly demonstrates the utility of the Ekman streamfunction in representing the wind-driven variability of the SOOC.

Data Availability Statement

The ACCESS-OM2-01 Interannual Forcing simulation model output (Kiss & Hogg, 2020) is part of the COSIMA Model Output Collection (COSIMA, 2020).

Acknowledgments
The authors acknowledge the support of this work from the Earth Systems and Climate Change Hub funded by the Australian Government's National Environmental Science Program (NESP). Many thanks to N. Constantinou, R. Holmes, and A. Morrison for very helpful discussions, and to COSIMA (http://www.cosima.org.au) for making available the ACCESS-OM2 suite of models. The numerical simulations and analysis were performed with the Gadi Supercomputer and Virtual Desktop Infrastructure resources of the National Computational Infrastructure (NCI Australia, 2013, 2019). The authors also thank Y. Kostov and J. Zika for their valuable reviews and suggestions which substantially improved our manuscript.

References

COSIMA. (2020). *Consortium for ocean-sea-ice modeling in Australia model output collection*. https://doi.org/10.4225/41/5a2dc8543105a
Döös, K., & Webb, D. (1994). The Deacon cell and other meridional cells of the Southern Ocean. *Journal of Physical Oceanography*, *24*, 429–442. https://doi.org/10.1175/1520-0485(1994)024<0429:tdcato>2.0.co;2
Downes, S., & Hogg, A. (2013). Southern Ocean circulation and eddy compensation in CMIP5 models. *Journal of Climate*, *26*, 7198–7220. https://doi.org/10.1175/JCLI-D-12-00504.1
Farneti, R., Downes, S., Griffies, S., Marsland, S., Behrens, E., Bentsen, M., et al. (2015). An assessment of Antarctic Circumpolar Current and Southern Ocean meridional overturning circulation during 1958–2007 in a suite of interannual CORE-II simulations. *Ocean Modeling*, *93*, 84–120. https://doi.org/10.1016/j.ocemod.2015.07.009
Gent, P. (2016). Effects of Southern Hemisphere wind changes on the meridional overturning circulation in ocean models. *Annual Review of Marine Science*, *8*, 79–94. https://doi.org/10.1146/annurev-marine-122414-033929
Goyal, R., Sen Gupta, A., Jucker, M., & England, M. (2021). Historical and projected changes in the Southern Hemisphere surface westerlies. *Geophysical Research Letters*, *48*, e2020GL090849. https://doi.org/10.1029/2020GL090849
Johnson, H., Cessi, P., Marshall, D., Schloesser, F., & Spall, M. (2019). Recent contributions of theory to our understanding of the Atlantic meridional overturning circulation. *Journal of Geophysical Research: Oceans*, *124*, 5376–5399. https://doi.org/10.1029/2019JC015330
Karsten, R., & Marshall, J. (2002). Constructing the residual circulation of the ACC from observations. *Journal of Physical Oceanography*, *32*, 3315–3327. https://doi.org/10.1175/1520-0485(2002)032<3315:ctrcot>2.0.co;2
Kiss, A., & Hogg, A. (2020). ACCESS-OM2 0.1 degree global model output (interannual forcing simulation). *Geoscientific Model Development*, *13*(2), 401–442. https://doi.org/10.25914/608097cb3433f
Kiss, A., Hogg, A., Hannah, N., Dias, F., Brassington, G., Chamberlain, M., et al. (2020). ACCESS-OM2: A global ocean-sea-ice model at three resolutions. *Geoscientific Model Development*, *13*, 401–442. https://doi.org/10.5194/gmd-13-401-2020
Lee, M.-M., & Nurser, A. (2012). Eddy subduction and the vertical transport streamfunction. *Journal of Physical Oceanography*, *42*, 1762–1780. https://doi.org/10.1175/JPO-D-11-0219.1
Locarnini, R., Mishonov, A., Antonov, J., Boyer, T., Garcia, H., Baranova, O., et al. (2013). *World Ocean Atlas 2013, volume 1: Temperature*. (Vol. 73). NOAA Atlas NESDIS.
Marshall, G. (2003). Trends in the southern annular mode from observations and reanalyses. *Journal of Climate*, *16*, 4134–4143. https://doi.org/10.1175/1520-0442(2003)016<4134:titsam>2.0.co;2
Marshall, J., & Radko, T. (2003). Residual-mean solutions for the Antarctic Circumpolar Current and its associated overturning circulation. *Journal of Physical Oceanography*, *33*, 2341–2354. https://doi.org/10.1175/1520-0485(2003)033<2341:rsftac>2.0.co;2
Marshall, J., & Speer, K. (2012). Closure of the meridional overturning circulation through Southern Ocean upwelling. *Nature Geoscience*, *5*, 171–180. https://doi.org/10.1038/NGEO1391
Mazloff, M., Ferrari, R., & Schneider, T. (2013). The force balance of the Southern Ocean meridional overturning circulation. *Journal of Physical Oceanography*, *43*, 1193–1208. https://doi.org/10.1175/JPO-D-12-069.1
NCI Australia. (2013). *Virtual desktop infrastructure*. https://doi.org/10.25914/608bfd1378fad
NCI Australia. (2019). *Gadi supercomputer*. https://doi.org/10.25914/608bfd1838db2
Olbers, D., & Visbeck, M. (2005). A model of the zonally averaged stratification and overturning in the Southern Ocean. *Journal of Physical Oceanography*, *35*, 1190–1205. https://doi.org/10.1175/JPO2750.1
Roemmich, D., Church, J., Gilson, J., Monselesan, D., Sutton, P., & Wijffels, S. (2015). Unabated planetary warming and its ocean structure since 2006. *Nature Climate Change*, *5*, 240–245. https://doi.org/10.1038/nclimate2513
Sabine, C., Feely, R., Gruber, N., Key, R., Lee, K., Bullister, J., et al. (2004). The oceanic sink for anthropogenic CO_2. *Science*, *305*, 367–371. https://doi.org/10.1126/science.1097403
Sallèe, J. (2018). Southern Ocean warming. *Oceanography*, *32*, 52–62. https://doi.org/10.5670/oceanog.2018.215
Sallèe, J., Speer, K., Rintoul, S., & Wijffels, S. (2010). Southern Ocean thermocline ventilation. *Journal of Physical Oceanography*, *40*, 509–529. https://doi.org/10.1175/2009JPO4291.1

Santer, B., Wigley, T., Boyle, J., Gaffen, D., Hnilo, J., Nychka, D., et al. (2000). Statistical significance of trends and trend differences in layer-average atmospheric temperature time series. *Journal of Geophysical Research: Atmospheres*, *105*, 7337–7356. https://doi.org/10.1029/1999JD901105

Speer, K., Rintoul, S., & Sloyan, B. (2000). The diabatic Deacon cell. *Journal of Physical Oceanography*, *30*, 3212–3222. https://doi.org/10.1175/1520-0485(2000)030<3212:tddc>2.0.co;2

Stewart, K., & Hogg, A. (2019). Southern Ocean heat and momentum uptake are sensitive to the vertical resolution at the ocean surface. *Ocean Modeling*, *143*, 101456. https://doi.org/10.1016/j.ocemod.2019.101456

Stewart, K., Hogg, A., Griffies, S., Heerdegen, A., Ward, M., Spence, P., & England, M. (2017). Vertical resolution of baroclinic modes in global ocean models. *Ocean Modeling*, *113*, 50–65. https://doi.org/10.1016/j.ocemod.2017.03.012

Swart, N., & Fyfe, J. (2012). Observed and simulated changes in the Southern Hemisphere surface westerly wind stress. *Geophysical Research Letters*, *39*, L16711. https://doi.org/10.1029/2012GL052810

Tandon, N., Saenko, O., Cane, M., & Kushner, P. (2020). Interannual variability of the global meridional overturning circulation dominated by pacific variability. *Journal of Physical Oceanography*, *50*, 559–574. https://doi.org/10.1175/JPO-D-19-0129.1

Toggweiler, J., & Samuels, B. (1995). Effect of Drake Passage on the global thermohaline circulation. *Deep-Sea Research I*, *42*, 477–500. https://doi.org/10.1016/0967-0637(95)00012-U

Treguier, A., England, M., Rintoul, S., Madec, G., Sommer, J. L., & Molines, J. (2007). Southern Ocean overturning circulation across streamlines in an eddying simulation of the Antarctic Circumpolar Current. *Ocean Science*, *3*, 491–507. https://doi.org/10.5194/os-3-491-2007

Tsujino, H., Urakawa, S., Griffies, S., Danabasoglu, G., Adcroft, A., Amaral, A., et al. (2020). Evaluation of global ocean-sea-ice model simulations based on the experimental protocols of the Ocean Model Intercomparison Project phase 2 (OMIP-2). *Geoscientific Model Development*, *13*, 3643–3708. https://doi.org/10.5194/gmd-13-3643-2020

Tsujino, H., Urakawa, S., Nakano, H., Small, R., Kim, W., Yeager, S., et al. (2018). JRA-55 based surface data set for driving ocean-sea-ice models (JRA55-do). *Ocean Modeling*, *130*, 79–139. https://doi.org/10.1016/j.ocemod.2018.07.002

Zika, J., England, M., & Sijp, W. (2012). The ocean circulation in thermohaline coordinates. *Journal of Physical Oceanography*, *42*, 708–724. https://doi.org/10.1175/JPO-D-11-0139.1

Zweng, M., Reagan, J., Antonov, J., Locarnini, R., Mishonov, A., Boyer, T., et al. (2013). *World Ocean Atlas 2013, volume 2: Salinity* (Vol. 74). NOAA Atlas NESDIS.